

PHOTONICS Research

Comparison of growth structures for continuous-wave electrically pumped 1.55 μm quantum dash lasers grown on (001) Si

WEI LUO,^{1,2,†}  YING XUE,^{1,†}  JIE HUANG,¹ LIYING LIN,¹ BEI SHI,¹  AND KEI MAY LAU^{1,*} 

¹Department of Electronic and Computer Engineering, The Hong Kong University of Science and Technology, Clear Water Bay, Kowloon, Hong Kong, China

²e-mail: wluoag@connect.ust.hk

*Corresponding author: eekmlau@ust.hk

Received 28 July 2020; revised 4 October 2020; accepted 5 October 2020; posted 7 October 2020 (Doc. ID 403938); published 20 November 2020

Semiconductor lasers directly grown on silicon offer great potential as critical components in high-volume, low-cost integrated silicon photonics circuits. Although InAs/InP quantum dash (QDash) lasers on native InP substrate emitting at 1.5 μm (C-band) have demonstrated notable performance, the growth of InAs/InP QDash lasers on silicon remains undeveloped because of the 8% lattice mismatch between InP and silicon. Here we report advances of growth techniques leading to the first C-band room-temperature continuous-wave electrically pumped QDash lasers on CMOS standard (001) silicon substrates by metalorganic chemical vapor deposition. A correlation between various material characterizations and device performance is analyzed for different QDash laser structures grown on planar nominal (001) silicon. With the optimized QDash growth and improved fabrication process, the lowest threshold current density of 1.5 kA/cm^2 was determined on an 8 $\mu\text{m} \times 1.5 \text{ mm}$ device on planar silicon with a single facet output power exceeding 14 mW. The device results illustrate the good material quality of the QDash lasers grown on silicon, suggesting potential applications for other active components of photonic integrated circuits, such as semiconductor optical amplifiers, modulators, and photodetectors. © 2020 Chinese Laser Press

<https://doi.org/10.1364/PRJ.403938>

1. INTRODUCTION

The development of information technologies has fostered unprecedented data capacity transmitted and processed in data centers, local servers, and even personal devices. Silicon photonic integrated circuits, leveraging the well-established complementary metal-oxide semiconductor (CMOS) platform, are advantageous for their low cost, scalability, and large bandwidth capacity [1–5]. Among them, InP-based lasers emitting at long wavelengths are used for various applications such as communications, detection, and eye-safe LIDAR [6–8]. Although high-performance lasers on native III–V substrates have been transferred onto processed silicon wafers by bonding techniques [9–11], monolithic integration by direct growth on silicon offers an attractive alternative [12,13]. Work on III–V thin films grown on silicon for lasers has made tremendous progress over the past decades [14,15]. However, the growth of InP on silicon remains challenging due to the high defect density arising from the huge lattice mismatch between them. Growth techniques, including strained-layer superlattices (SLSs) and aspect ratio trapping, have been applied to improve the crystalline quality of InP on silicon [16].

Compared to conventional quantum well (QW) structures, three-dimensional confined quantum dots (QDs) and InAs/InP quantum dashes (QDashes) are less vulnerable to the propagating defects due to their strong carrier confinement and discrete distribution [17,18]. Other advantages of QD and QDash lasers, such as high temperature stability, large gain bandwidth, and low threshold current, have been reported [19]. InP-based QD or QDash lasers emitting in the telecom band have been demonstrated on III–V native substrate with impressive device performance [20–24]. Abdollahinia *et al.* demonstrated a low threshold current of $\sim 65 \text{ mA}$ at 20°C on an $893 \mu\text{m} \times 2.25 \mu\text{m}$ InAs QD laser on native InP substrate with facet coating [25]. And the characteristic temperature T_0 of the same size eight-layer QD laser is 144 K and 101 K in the range of $20\text{--}60^\circ\text{C}$ and $60\text{--}110^\circ\text{C}$, respectively. Based on the InP-on-silicon templates, our group has reported 1.55 μm QD lasers grown on silicon, including CW lasing of optically pumped QD lasers at 4.5 K and pulsed lasing of electrically pumped QD laser at room temperature over the past few years [26,27]. Recently, we demonstrated what we believe, to the best of our knowledge, is the first 1.55 μm room temperature

electrically pumped CW lasing of QDash lasers grown on silicon [28]. Here, we report an investigation of the laser performance with different structures, their as-grown material characteristics, and measured device results.

2. MATERIAL GROWTH AND QDASH STRUCTURE DESIGN

The electrically pumped InAs/InAlGaAs QDash laser structure was directly grown on commercial nominal (001) silicon (0.5° offcut angle along [110] direction measured in house) by metal-organic chemical vapor deposition (MOCVD). The defects generated in hetero-epitaxy, including threading dislocations (TDs), stacking faults (SFs), twins, and anti-phase boundaries (APBs), would degrade the device performance [29]. Different growth techniques were applied to address these defect issues. Prior to III–V buffer growth, 800°C annealing under H_2 ambient was initially performed to desorb the oxide and rearrange the silicon atoms on the surface, which was favorable to avoid the formation of APBs for III–V growth on silicon [30]. To accommodate the lattice mismatch between InP and silicon, a GaAs intermediate buffer was first grown on the silicon substrate [31,32]. The GaAs was grown at increasing temperatures in three steps, from 400°C , then 550°C , and 600°C . After the $1\text{ }\mu\text{m}$ GaAs growth, five cycles of thermal cycle annealing (TCA) were applied with temperature cycling between 330°C and 780°C , to reduce the defect density of GaAs and thus provide a less defective growth front for the following InP buffer [33]. The improved crystal quality is supported by the reduction of full width at half-maximum (FWHM) of the X-ray diffraction (XRD) rocking curve from 580 to 380 arcsec after TCA. A $10\text{ }\mu\text{m} \times 10\text{ }\mu\text{m}$ atomic force microscope (AFM) image of GaAs on planar silicon (GoPS) is shown in Fig. 1(a) and the root mean square (RMS) value of the surface roughness is 1.1 nm.

InP was subsequently grown on the GoPS with three-step temperature ramping, namely LT (445°C), MT (555°C), and HT (630°C). Three sets of 10-period 11.5 nm $\text{In}_{0.63}\text{Ga}_{0.37}\text{As}/31\text{ nm}$ InP SLs were inserted in the HT-InP as dislocation filters to reduce the threading dislocation densities (TDDs) [34,35]. Each set of SLs was separated by 250 nm of InP, and the total thickness of the InP buffer was 3.1 μm . A $10\text{ }\mu\text{m} \times 10\text{ }\mu\text{m}$ AFM image of the InP grown on GoPS is shown in Fig. 1(b) with an RMS value of 2.8 nm.

To obtain a numerical value of the defect density, plan-view transmission electron microscope (TEM) samples were prepared and 32 images were taken with each scanning area larger than $2.7\text{ }\mu\text{m} \times 2.7\text{ }\mu\text{m}$. A representative plan view TEM image is shown in Fig. 1(c). After statistical counting of these defects, the defect density of the InP/GoPS template is $3.6 \times 10^8\text{ cm}^{-2}$ with a standard deviation of $0.4 \times 10^8\text{ cm}^{-2}$.

Different structures shown in Fig. 2 were designed to optimize the laser structure of the QDashes. The 2.4 monolayer (ML) InAs QDashes were directly grown on an InGaAs strain layer and capped with LT-InGaAs or LT-InAlGaAs to form the dot-in-well (DWELL) structure [36]. Immediately after this, the temperature was ramped up and the exposed surface was further capped with an HT-InAlGaAs second cap layer (SCL). The QDash stacks were sandwiched by symmetrical InAlGaAs thin cladding layers that were lattice-matched to InP, to form separate confinement heterostructures (SCHs). The 30 nm InAlGaAs spacer was slightly lattice-mismatched to InP to balance the strain accumulated by the growth of QDashes, and the exposed QDash layer on top was grown for AFM characterization. All the structures were grown on the same InP/GoPS buffer for a fair comparison. In search of a proper balance of optical and carrier confinement, the Al composition in the InAlGaAs was adjusted in the design of the following QDash structures. As shown in the QDash laser structures in Fig. 2, the larger refractive index of InAlGaAs SCH provides better optical confinement, but the band offset between the InAlGaAs and QDash is reduced, leading to a decreased charge carrier confinement. The balance between the two effects was evaluated with the overall device performance. Sample A in Fig. 2(a) follows our previous structure for a 1.5 μm QDash laser with the Al composition of InAlGaAs changed from 0.29 to 0.24 to increase the refractive index of the SCH [27]. In Sample B, the LT-InAlGaAs cap was replaced by LT-InGaAs to form a symmetric DWELL structure based on Sample A. In Sample C, the Al composition of InAlGaAs layer was changed back to 0.29, with an increase of the InAlGaAs barrier thickness from 200 nm to 300 nm to enhance optical confinement based on Sample B. Compared to Sample B, better charge carrier confinement is achieved by changing the bandgap of InAlGaAs in Sample C. Electrically pumped laser structures with these three different active regions were grown on previously described

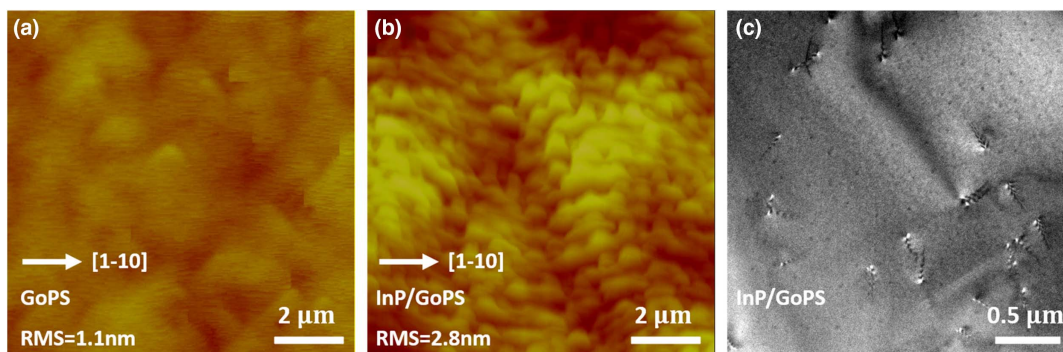


Fig. 1. (a) AFM image of 1.1 μm GaAs on planar silicon after TCA, and RMS of the $10\text{ }\mu\text{m} \times 10\text{ }\mu\text{m}$ area is 1.1 nm. (b) AFM image of 3.1 μm InP on GoPS, and RMS of the $10\text{ }\mu\text{m} \times 10\text{ }\mu\text{m}$ area is 2.8 nm. (c) Representative plan view TEM image of InP on GoPS.

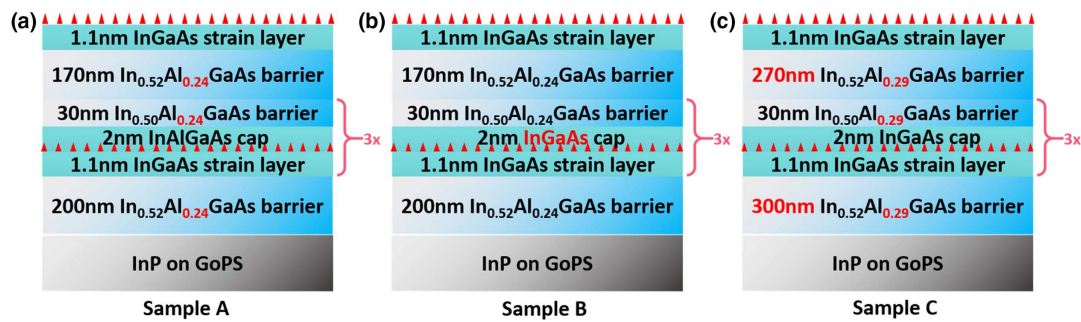


Fig. 2. Schematic diagram of QDashes grown on InP/GoPS with different structures. (a) Sample A: Al composition of InAlGaAs is changed from 0.29 to 0.24. (b) Sample B: low temperature cap layer is changed from InAlGaAs to InGaAs based on Sample A. (c) Sample C: Al composition of InAlGaAs is changed back to 0.29, and the thickness of InAlGaAs is increased from 200 nm to 300 nm based on Sample B.

InP/GoPS templates. The growth sequence was as follows: 600 nm n-type InP contact layer, 630 nm n-type InP cladding, three-stack QDash active region, 1500 nm p-type InP cladding, and 140 nm p-type InGaAs contact layer. The doping concentration of the n-type InP contact and the cladding layer is $5 \times 10^{18} \text{ cm}^{-3}$ and $5.5 \times 10^{17} \text{ cm}^{-3}$, respectively. And the doping concentration of the p-type InP cladding and the InGaAs contact layer is $9 \times 10^{17} \text{ cm}^{-3}$ and $1.6 \times 10^{19} \text{ cm}^{-3}$, respectively.

3. RESULTS AND DISCUSSION

A. Material Characterization

From the global view cross-section TEM of the InP/GoPS template shown in Fig. 3(a), the defects originated from the InP/GaAs hetero-epitaxy interface are effectively trapped by the inserted SLSs. On top of the InP/GoPS, different QDash structures were grown with additional top layer QDashes exposed for AFM characterization, which unveils the morphology and density of the QDashes. An example is presented in Fig. 3(b).

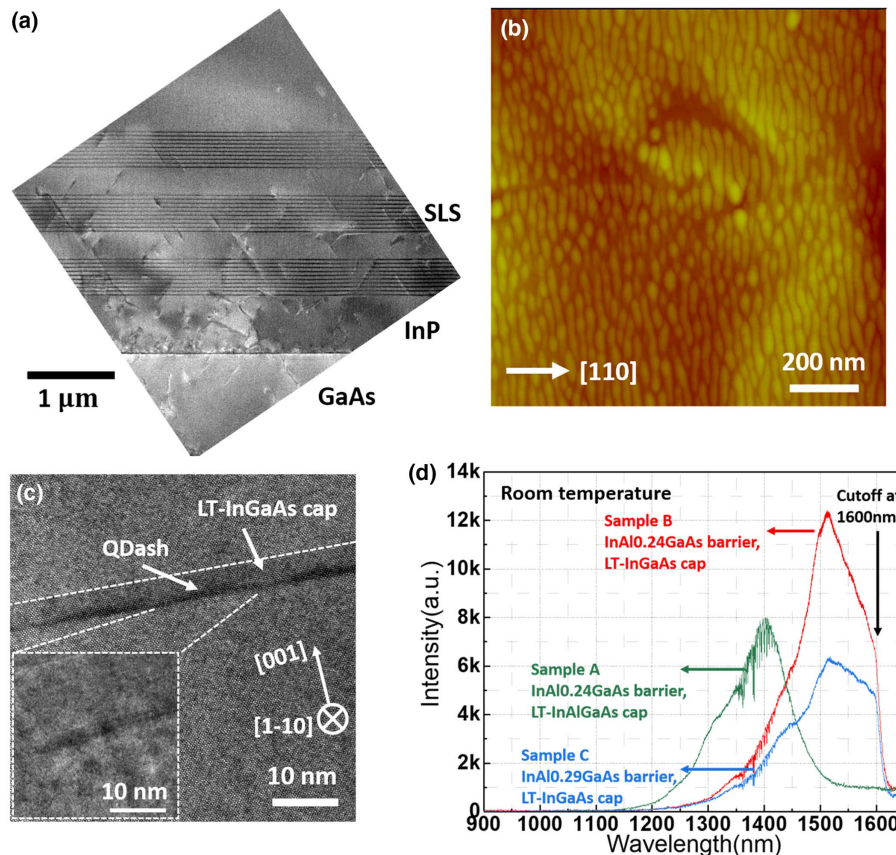


Fig. 3. (a) Cross-section TEM image of InP/GoPS template. (b) $1 \mu\text{m} \times 1 \mu\text{m}$ AFM image of top exposed QDashes grown on InP/GoPS (Sample B). (c) Cross-section TEM image of QDashes grown on InP/GoPS with zoomed-in image as inset. (d) Room temperature PL of three-layer QDashes grown on Samples A, B, and C. The measurement was cutoff at 1600 nm due to the photodetector.

The QDashes are elongated along the [1–10] direction, and the estimated QDashes density from the AFM image is approximately $3.5 \times 10^{10} \text{ cm}^{-2}$. A cross-section TEM image of the QDashes within the full laser structure is shown in Fig. 3(c) with a higher resolution QDash image in the inset. The room temperature PL spectra of the QDashes excited by a CW 514 nm laser are shown in Fig. 3(d).

The PL difference between Samples A and B is attributed to the low-temperature cap layer. Compared to InAlGaAs, InGaAs reduces the energy gap between the cap layer and QDashes, thereby causing a red shift of the PL peak wavelength in Sample B [37]. The elimination of Al in the cap layer helps to reduce the impurities, which accounts for the increased PL intensity in Sample B. In addition, by changing the low-temperature cap layer with little composition difference, the local strain of QDashes is also modified, which influences the morphology and emitting wavelength of QDashes [38,39]. The Al composition and thickness of the InAlGaAs barriers are different in Samples B and C. In Sample B, the Al composition is smaller, resulting in a smaller bandgap ($\sim 1.1 \text{ eV}$) and a larger refractive index (~ 3.36) [40,41]. InAlGaAs with a larger refractive index offers better optical confinement for the emitting light, while the relatively smaller bandgap of InAlGaAs could decrease the charge carrier confinement with a reduced conduction band offset between the InAlGaAs and QDashes. Therefore, the Al fraction inside the InAlGaAs alloy is a trade-off in balancing the carrier and photon confinement. In our experiment, the sample with the Al composition of InAlGaAs at 0.24 led to a more desirable PL spectrum. The PL intensity of Sample B is twice higher than that of Sample C without wavelength shifting. Sample B with an InGaAs LT-cap and $\text{In}_{0.52}\text{Al}_{0.24}\text{Ga}_{0.24}\text{As}$ barrier exhibits the best PL performance among these three samples.

B. Device Performance

To investigate the device performance of the samples with these three structures, we fabricated ridge waveguide edge-emitting lasers. As illustrated in Fig. 4(a), the first ridge mesa stops right above the active region and the second mesa is terminated at the n-contact InP layer. The process was completed using conventional photolithography and dry etch steps. The fabricated samples were thinned down to around $100 \mu\text{m}$ by

substrate lapping and cleaved into laser bars with the facets uncoated. A 70° tilted scanning electron microscope (SEM) image of a finished device ($6 \mu\text{m}$ ridge width) on planar silicon is displayed in Fig. 4(b) with the GaAs slightly wet etched to enhance the contrast. The clean and mirror-like as-cleaved facet guarantees a low optical loss of the laser cavity.

The laser bars were placed on a heat sink with a temperature controller and tested at various temperatures. The device performance was characterized under both pulsed current drive and continuous current drive for comparison. A duty cycle of 0.5% and a pulse width of 400 ns were used for the pulsed measurements. The current–voltage (I–V) characteristics were similar for the devices on these three samples. The typical turn-on voltage of 0.7 V and series resistance of around $5\text{--}9 \Omega$ were measured as shown in the representative I–V curves in Fig. 5(a). For the light-current (L–I) characterization at 25°C , the lasers on Samples B and C could both be CW, but the lasers on Sample A could only be pulsed. The pulsed L–I curves of the different sized lasers on Sample A are shown in Fig. 5(b). When comparing Samples B and C under CW electrical pumping, lasers on Sample B demonstrated a lower threshold current density with the same device dimensions as presented in Fig. 5(c). The results agree well with the earlier PL measurement. To evaluate the laser performance at elevated temperatures, the devices on these three samples were tested with an increased stage temperature under pulsed electrical pumping. The threshold currents of the devices with a $6 \mu\text{m}$ ridge width and 1 mm cavity length on these three samples are shown in Fig. 5(d) as a function of temperature. Compared to the characteristic temperature T_0 of QD laser on native InP substrate [25], the smaller T_0 value here may be caused by the imperfect InP-on-Si buffer quality, which introduces the nonradiative recombination centers in the active region. The devices on Sample B show the lowest threshold current as well as the highest characteristic temperature with the pulsed operation temperature up to 90°C . To sum up, both the material characterization and device performance seem to indicate the structure of Sample B with the InGaAs LT-cap and $\text{In}_{0.52}\text{Al}_{0.24}\text{Ga}_{0.24}\text{As}$ barrier is better than the other two.

In addition to the study of the active region, we also improved our fabrication process and adopted a deep-etched structure with the ridge etched through the active region in

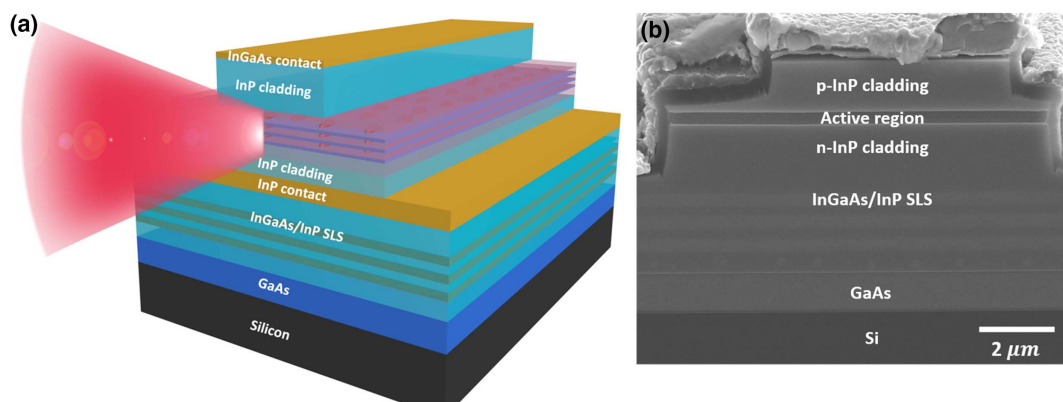


Fig. 4. (a) Schematic diagram (not to scale) and (b) 70° tilted cross-section SEM image of a fabricated Fabry–Pérot (FP) laser on InP/GoPS.

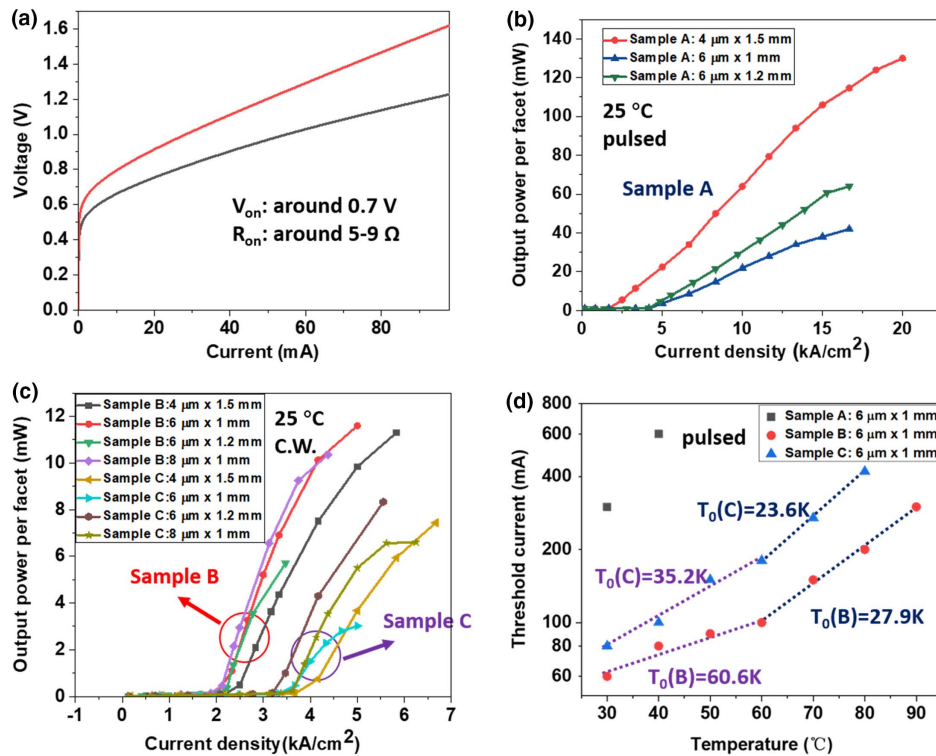


Fig. 5. (a) Representative I–V curves of fabricated devices with turn-on voltage of around 0.7 V. (b) Room temperature pulsed lasing L–I curves of different size FP lasers on Sample A. (c) Room temperature continuous-wave lasing L–I curves of different size FP lasers on Samples B and C. (d) Pulsed lasing threshold currents of 6 $\mu\text{m} \times 1\text{ mm}$ lasers on Samples A, B, and C at different temperatures.

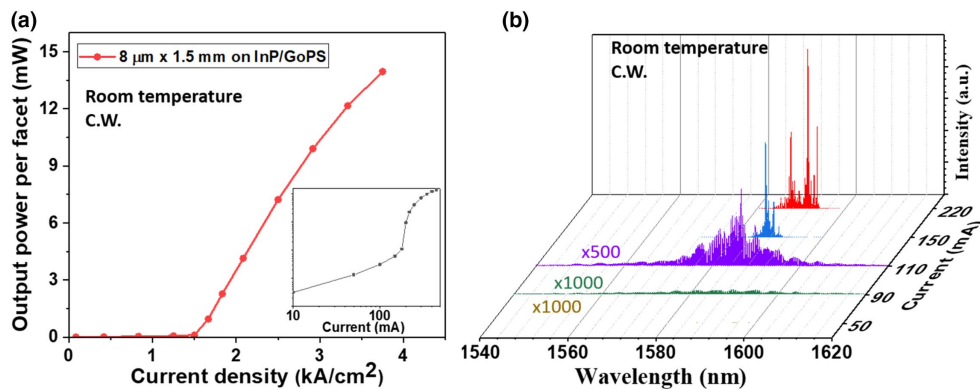


Fig. 6. (a) L–I curve of an 8 $\mu\text{m} \times 1.5\text{ mm}$ deep-etched FP laser on Sample B with the lowest threshold current density of 1.5 kA/cm^2 under CW lasing at room temperature. Inset is the L–I curve plotted in logarithmic scale. (b) Room temperature CW lasing spectrum of a deep-etched FP laser on Sample B.

one step for better device performance [28]. Figure 6(a) shows the L–I curve of a device with an 8 μm ridge width and 1.5 mm cavity length on Sample B, which presents the lowest threshold current density of 1.5 kA/cm^2 under CW operation. The L–I curve is also plotted in a logarithmic scale in the inset of Fig. 6(a), which demonstrates an “S-shaped” nonlinear transition from spontaneous to stimulated emission. The electroluminescence (EL) spectra shown in Fig. 6(b) demonstrate multimode lasing with the primary peak located at 1580 nm. Multimode lasing is observed due to the large size of the FP laser, which

supports many modes in the FP cavity. The laser can pulsed lase up to 95 °C. More static characteristics of the QDash laser on InP-on-Si and native InP substrate are studied in Ref. [28].

4. CONCLUSION

In conclusion, we have demonstrated room-temperature CW lasing of electrically pumped InAs/InAlGaAs QDash lasers monolithically grown on (001) silicon emitting at the C band. A comparison of three different QDash structures

is discussed in terms of material quality and device performance. The QDash structure with the LT-InGaAs cap and $\text{In}_{0.52}\text{Al}_{0.24}\text{Ga}_{0.24}\text{As}$ barrier is favorable. Based on the optimized QDash structure and fabrication process, the lowest threshold current density of 1.5 kA/cm^2 is obtained on an $8 \mu\text{m} \times 1.5 \text{ mm}$ device. This work also shows that the quality of the large lattice-mismatched epitaxy of InP-on-silicon template is good enough to support the CW operation of lasers at room temperature. Future work would be focused on the further improvement of the InP-on-silicon buffer quality and the density of QDashes for better device performance.

Funding. Research Grants Council, University Grants Committee (614813, 16212115); Innovation and Technology Fund (ITS/273/16FP).

Acknowledgment. The author would like to thank the Nanosystem Fabrication Facility (NFF) and the Material Characterization & Preparation Facility (MCPF) of HKUST for technical support and discussion, Prof. Peter M. Smowton for growth suggestions, and Si Zhu, Yu Han, Zhao Yan, and Chak Wah Tang for fruitful discussions.

Disclosures. The authors declare no conflicts of interest.

[†]These authors contributed equally to this work.

REFERENCES

- D. Liang and J. E. Bowers, "Recent progress in lasers on silicon," *Nat. Photonics* **4**, 511–517 (2010).
- M. Hochberg and T. Baehr-Jones, "Towards fabless silicon photonics," *Nat. Photonics* **4**, 492–494 (2010).
- M. Asghari and A. V. Krishnamoorthy, "Energy-efficient communication," *Nat. Photonics* **5**, 268–270 (2011).
- D. Liang, X. Huang, G. Kurczveil, M. Fiorentino, and R. G. Beausoleil, "Integrated finely tunable microring laser on silicon," *Nat. Photonics* **10**, 719–722 (2016).
- D. Thomson, A. Zilkie, J. E. Bowers, T. Komljenovic, G. T. Reed, L. Vivien, D. Marris-Morini, E. Cassan, L. Viot, J.-M. Féféli, J.-M. Hartmann, J. H. Schmid, D.-X. Xu, F. Boeuf, P. O'Brien, G. Z. Mashanovich, and M. Nedeljkovic, "Roadmap on silicon photonics," *J. Opt.* **18**, 073003 (2016).
- T. Septon, A. Becker, S. Gosh, G. Shtendel, V. Sichkovskiy, F. Schnabel, A. Sengül, M. Bjelica, B. Witzigmann, J. P. Reithmaier, and G. Eisenstein, "Large linewidth reduction in semiconductor lasers based on atom-like gain material," *Optica* **6**, 1071–1077 (2019).
- Y. Jiao, B. W. Tilma, J. Kotani, R. Nötzel, M. K. Smit, S. He, and E. A. J. M. Bente, "InAs/InP(100) quantum dot waveguide photodetectors for swept-source optical coherence tomography around $1.7 \mu\text{m}$," *Opt. Express* **20**, 3675–3692 (2012).
- C. Yu, J. Qiu, H. Xia, X. Dou, J. Zhang, and J.-W. Pan, "Compact and lightweight $1.5 \mu\text{m}$ lidar with a multi-mode fiber coupling free-running InGaAs/InP single-photon detector," *Rev. Sci. Instrum.* **89**, 103106 (2018).
- N. Fujioka, T. Chu, and M. Ishizaka, "Compact and low power consumption hybrid integrated wavelength tunable laser module using silicon waveguide resonators," *J. Lightwave Technol.* **28**, 3115–3120 (2010).
- J. Justice, C. Bower, M. Meitl, M. B. Mooney, M. A. Gubbins, and B. Corbett, "Wafer-scale integration of group III–V lasers on silicon using transfer printing of epitaxial layers," *Nat. Photonics* **6**, 610–614 (2012).
- M. J. R. Heck, J. F. Bauters, M. L. Davenport, J. K. Doyle, S. Jain, G. Kurczveil, S. Srinivasan, Y. Tang, and J. E. Bowers, "Hybrid silicon photonic integrated circuit technology," *IEEE J. Sel. Top. Quantum Electron.* **19**, 6100117 (2013).
- D. Huang, M. A. Tran, J. Guo, J. Peters, T. Komljenovic, A. Malik, P. A. Morton, and J. E. Bowers, "High-power sub-kHz linewidth lasers fully integrated on silicon," *Optica* **6**, 745–752 (2019).
- Y. Zhang, Q. Du, C. Wang, T. Fakhru, S. Liu, L. Deng, D. Huang, P. Pintus, J. Bowers, C. A. Ross, J. Hu, and L. Bi, "Monolithic integration of broadband optical isolators for polarization-diverse silicon photonics," *Optica* **6**, 473–478 (2019).
- D. Jung, P. G. Callahan, B. Shin, K. Mukherjee, A. C. Gossard, and J. E. Bowers, "Low threading dislocation density GaAs growth on on-axis GaP/Si (001)," *J. Appl. Phys.* **122**, 225703 (2017).
- B. Shi, Q. Li, and K. M. Lau, "Self-organized InAs/InAlGaAs quantum dots as dislocation filters for InP films on (001) Si," *J. Cryst. Growth* **464**, 28–32 (2017).
- B. Shi, H. Zhao, L. Wang, B. Song, S. T. Suran Brunelli, and J. Klamkin, "Continuous-wave electrically pumped 1550 nm lasers epitaxially grown on on-axis (001) silicon," *Optica* **6**, 1507–1514 (2019).
- Z. Liu, C. Hantschmann, M. Tang, Y. Lu, J.-S. Park, M. Liao, S. Pan, A. Sanchez, R. Beanland, M. Martin, T. Baron, S. Chen, A. Seeds, R. Penty, I. White, and H. Liu, "Origin of defect tolerance in InAs/GaAs quantum dot lasers grown on silicon," *J. Lightwave Technol.* **38**, 240–248 (2020).
- S. Chen, W. Li, J. Wu, Q. Jiang, M. Tang, S. Shutts, S. N. Elliott, A. Sobiesierski, A. J. Seeds, I. Ross, P. M. Smowton, and H. Liu, "Electrically pumped continuous-wave III–V quantum dot lasers on silicon," *Nat. Photonics* **10**, 307–311 (2016).
- T. Sadeev, D. Arsenijević, and D. Bimberg, "Comparison of dynamic properties of InP/InAs quantum-dot and quantum-dash lasers," *Appl. Phys. Lett.* **109**, 161104 (2016).
- R. Rosales, K. Merghem, A. Martinez, A. Akrou, J.-P. Tournenc, A. Accard, F. Lelarge, and A. Ramdane, "InAs/InP quantum-dot passively mode-locked lasers for $1.55\text{-}\mu\text{m}$ applications," *IEEE J. Sel. Top. Quantum Electron.* **17**, 1292–1301 (2011).
- D. Gready, G. Eisenstein, V. Ivanov, C. Gilfert, F. Schnabel, A. Rippien, J. P. Reithmaier, and C. Bornholdt, "High speed $1.55 \mu\text{m}$ InAs/InGaAlAs/InP quantum dot lasers," *IEEE Photon. Technol. Lett.* **26**, 11–13 (2014).
- J. Duan, H. Huang, Z. G. Lu, P. J. Poole, C. Wang, and F. Grillot, "Narrow spectral linewidth in InAs/InP quantum dot distributed feedback lasers," *Appl. Phys. Lett.* **112**, 121102 (2018).
- G. Liu, Z. Lu, J. Liu, Y. Mao, M. Vachon, C. Song, P. Barrios, and P. J. Poole, "Passively mode-locked quantum dash laser with an aggregate 5376 Tbit/s PAM-4 transmission capacity," *Opt. Express* **28**, 4587–4593 (2020).
- E. Alkhazraji, M. S. Alias, K. K. Qureshi, and M. Z. M. Khan, "Monolithic tunable InAs/InP broadband quantum-dash laser," *IEEE Access* **8**, 39046–39055 (2020).
- A. Abdollahinia, S. Banyoudeh, A. Rippien, F. Schnabel, O. Eyal, I. Cestier, I. Kalifa, E. Mentovich, G. Eisenstein, and J. P. Reithmaier, "Temperature stability of static and dynamic properties of $1.55 \mu\text{m}$ quantum dot lasers," *Opt. Express* **26**, 6056–6066 (2018).
- B. Shi, S. Zhu, Q. Li, Y. Wan, E. L. Hu, and K. M. Lau, "Continuous-wave optically pumped $1.55 \mu\text{m}$ InAs/InAlGaAs quantum dot micro-disk lasers epitaxially grown on silicon," *ACS Photon.* **4**, 204–210 (2017).
- S. Zhu, B. Shi, and K. M. Lau, "Electrically pumped $1.5 \mu\text{m}$ InP-based quantum dot microring lasers directly grown on (001) Si," *Opt. Lett.* **44**, 4566–4569 (2019).
- Y. Xue, W. Luo, S. Zhu, L. Lin, B. Shi, and K. M. Lau, " $1.55 \mu\text{m}$ electrically pumped continuous wave lasing of quantum dash lasers grown on silicon," *Opt. Express* **28**, 18172–18179 (2020).
- D. Jung, R. Herrick, J. Norman, K. Turnlund, C. Jan, K. Feng, A. C. Gossard, and J. E. Bowers, "Impact of threading dislocation density on the lifetime of InAs quantum dot lasers on Si," *Appl. Phys. Lett.* **112**, 153507 (2018).
- R. Alcotte, M. Martin, J. Moeyaert, R. Cipro, S. David, F. Bassani, F. Ducroquet, Y. Bogumilowicz, E. Sanchez, Z. Ye, X. Y. Bao, J. B. Pin, and T. Baron, "Epitaxial growth of antiphase boundary free GaAs layer

- on 300 nm Si(001) substrate by metalorganic chemical vapour deposition with high mobility," *APL Mater.* **4**, 046101 (2016).
31. H. Horikawa, Y. Kawai, M. Akiyama, and M. Sakuta, "Hetero-epitaxial growth of InP on Si substrates by LP-MOVPE," *J. Cryst. Growth* **93**, 523–526 (1988).
 32. M. K. Lee, D. S. Wu, H. H. Tung, K. Y. Yu, and K. C. Huang, "Characterization of InP/GaAs epilayers grown on Si substrates by low-pressure organometallic vapor phase epitaxy," *Appl. Phys. Lett.* **52**, 880–882 (1988).
 33. M. Yamaguchi, A. Yamamoto, M. Tachikawa, Y. Itoh, and M. Sugo, "Defect reduction effects in GaAs on Si substrates by thermal annealing," *Appl. Phys. Lett.* **53**, 2293–2295 (1988).
 34. T. Ward, A. M. Sánchez, M. Tang, J. Wu, H. Liu, D. J. Dunstan, and R. Beanland, "Design rules for dislocation filters," *J. Appl. Phys.* **116**, 063508 (2014).
 35. L. Megalini, S. Šuran Brunelli, W. Charles, A. Taylor, B. Isaac, J. Bowers, and J. Klamkin, "Strain-compensated InGaAsP superlattices for defect reduction of InP grown on exact-oriented (001) patterned Si substrates by metal organic chemical vapor deposition," *Materials* **11**, 337 (2018).
 36. A. Lee, Q. Jiang, M. Tang, A. Seeds, and H. Liu, "Continuous-wave InAs/GaAs quantum-dot laser diodes monolithically grown on Si substrate with low threshold current densities," *Opt. Express* **20**, 22181–22187 (2012).
 37. T. Sugaya, S. Furue, H. Komaki, T. Amano, M. Mori, K. Komori, S. Niki, O. Numakami, and Y. Okano, "Highly stacked and well-aligned $\text{In}_{0.4}\text{Ga}_{0.6}\text{As}$ quantum dot solar cells with $\text{In}_{0.2}\text{Ga}_{0.8}\text{As}$ cap layer," *Appl. Phys. Lett.* **97**, 183104 (2010).
 38. N.-T. Yeh, T.-E. Nee, J.-I. Chyi, T. M. Hsu, and C. C. Huang, "Matrix dependence of strain-induced wavelength shift in self-assembled InAs quantum-dot heterostructures," *Appl. Phys. Lett.* **76**, 1567–1569 (2000).
 39. P. Hazdra, J. Oswald, V. Komarnitskyy, K. Kuldová, A. Hospodková, E. Hulcius, and J. Pangrác, "Self-assembled InAs/GaAs quantum dots covered by different strain reducing layers exhibiting strong photo- and electroluminescence in 1.3 and 1.55 μm bands," *J. Nanosci. Nanotechnol.* **11**, 6804–6809 (2011).
 40. Y.-A. Chang, J.-R. Chen, H.-C. Kuo, Y.-K. Kuo, and S.-C. Wang, "Theoretical and experimental analysis on InAlGaAs/AlGaAs active region of 850-nm vertical-cavity surface-emitting lasers," *J. Lightwave Technol.* **24**, 536–543 (2006).
 41. M. J. Mondry, D. I. Babic, J. E. Bowers, and L. A. Coldren, "Refractive indexes of (Al, Ga, In)As epilayers on InP for optoelectronic applications," *IEEE Photon. Technol. Lett.* **4**, 627–630 (1992).